

# Numerical Simulation of Boundary Layer Ingesting (BLI) Inlet/Fan Interaction

James Giuliani<sup>1</sup> and Jen-Ping Chen<sup>2</sup>  
*The Ohio State University, Columbus, OH, 43221*

Timothy Beach  
*Coyote Hollow Consulting LLC, Walton Hills, Ohio 44146*

Milind Bakhle<sup>3</sup>  
*NASA Glenn Research Center, Cleveland, OH, 44135*

Future civil transport designs may incorporate engine inlets integrated into the body of the aircraft to take advantage of efficiency increases due to weight and drag reduction. Additional increases in engine efficiency are predicted if the inlet ingests the lower momentum boundary layer flow. Previous studies have shown, however, that efficiency benefits of Boundary Layer Ingesting (BLI) ingestion are very sensitive to the magnitude of fan and duct losses, and blade structural response to the non-uniform flow field that results from a BLI inlet has not been studied in-depth. This paper presents an effort to extend the modeling capabilities of an existing rotating turbomachinery unsteady analysis code to include the ability to solve the external and internal flow fields of a BLI inlet. The TURBO code has been a successful tool in evaluating fan response to flow distortions for traditional engine/inlet integrations, such as the development of rotating stall and inlet distortion through compressor stages. This paper describes the first phase of an effort to extend the TURBO model to calculate the external and inlet flowfield upstream of fan so that accurate pressure distortions that result from BLI configurations can be computed and used to analyze fan aerodynamics and structural response. To validate the TURBO program modifications for the BLI flowfield, experimental test data obtained by NASA for a flush-mounted S-duct with large amounts of boundary layer ingestion was modeled. Results for the flow upstream and in the inlet are presented and compared to experimental data for several high Reynolds number flows to validate the modifications to the solver. Quantitative data is presented that indicates good predictive capability of the model in the upstream flow. A representative fan is attached to the inlet and results are presented for the coupled inlet/fan model. The impact on the total pressure distortion at the AIP after the fan is attached is examined.

## Nomenclature

$AIP$	= Aerodynamic Interface Plane
$A_i$	= Inlet throat area
$A_o$	= Inlet mass-flow streamtube area at freestream conditions
$A_c$	= Inlet capture area
$BLI$	= Boundary Layer Ingesting
$D_2$	= diameter of the inlet at the AIP
$M_\infty$	= Tunnel/external Mach number
$P_{t,\infty}$	= Tunnel/external total pressure

---

<sup>1</sup> Senior Systems Manager and Graduate Student, Mechanical and Aerospace Engineering Dept., The Ohio State University, 201 W. 19<sup>th</sup> Ave., Columbus, OH 43210, AIAA Student Member.

<sup>2</sup> Associate Professor, Mechanical and Aerospace Engineering Dept., The Ohio State University, 201 W. 19<sup>th</sup> Ave., Columbus, OH 43210, AIAA Senior Member.

<sup>3</sup> Aerospace Engineer, Multiscale and Multiphysics Modeling Branch, AIAA Associate Fellow.

$T_{t,\infty}$	=	Tunnel/external total temperature
$Re$	=	Reynolds Number
$\dot{m}_{2c}$	=	Massflow at the AIP
$i$	=	Axial cell index
$j$	=	Radial cell index
$k$	=	Circumferential cell index
$q$	=	Numerical solution vector
$q_{cl}$	=	Solution at centerline point

## I. Introduction

Previous studies<sup>1,2</sup> have shown that the efficiency benefits of propulsion systems that ingest significant amounts of boundary layer are sensitive to the magnitude of duct and compressor losses. Seven categories of physical phenomena were classified as having an impact on the benefits of Boundary Layer Ingesting (BLI) inlets<sup>2</sup>. These included the state of the boundary layer entering the inlet, the inlet design, evolution of the flow in the inlet, distortion transfer across the fan, response of the fan to the distortion, evolution of the flow downstream of the fan and duct losses. Current engine installations that divert or bleed off the boundary layer entering the inlet are designed to operate over a wide range of operating conditions and angles of attack. BLI designs will need to meet or exceed these operating parameters and the boundary layer entering the inlet can be significantly impacted by off-design operating conditions. A high fidelity model is therefore needed to more accurately calculate inlet/engine performance for aircraft design studies, and to examine the blade response to the distorted flow field.

Numerous analytical and numerical techniques have been used to analyze combinations of the above phenomena. Several efforts have approached the problem by modeling individual components with appropriate boundary conditions<sup>3,4</sup>. Recently, work has been published where solutions of the entire flow field including both inlet and fan<sup>5,6</sup> have been undertaken in an effort to improve the accuracy of the distortion calculation and its transfer to the fan.

Since the primary goal of this effort is accurate prediction of the fan response to non-uniform flow fields generated by BLI inlets, the TURBO code<sup>7</sup> was selected as the base for the model so that the wealth of experience and anchoring of the code to turbomachinery applications can be used to provide increased confidence in the computations of the complex fan/compressor flow field. The numerical scheme already has many of the capabilities to model the external flow and inlet flow fields and will be extended to model the upstream flows in addition to the fan section. To validate the upstream predictive abilities of the modified code, an experimental BLI inlet geometry<sup>8</sup> that was tested at NASA Langley under the Blended Wing Body program, will be modeled with the modified TURBO. By validating the external and inlet flow fields, combined with the previous validation of TURBO axial machinery solutions, high confidence can be gained in applying the coupled model to new design geometries and operating conditions.

## II. Numerical Model

The TURBO program is a physics-based simulation tool for multistage turbomachinery. The solver computes the fluid conservation laws without ad hoc modeling of any flow phenomenon other than models required for turbulence. This code solves the unsteady Reynolds averaged Navier–Stokes equations and a decoupled  $k-\epsilon$  turbulence model. The code is implemented in a portable, scalable form for distributed-memory parallel computers using Message Passing Interface (MPI). The parallel implementation employs domain decomposition and supports general multi-block grids with arbitrary grid-block connectivity. The solution algorithm is a Newton iterative implicit time-accurate scheme with characteristics-based finite-volume spatial discretization. The Newton sub-iterations are solved using a concurrent block-Jacobi symmetric Gauss–Seidel (BJ-SGS) relaxation scheme. Because all of the fundamental fluid mechanics are computed, the code is capable of capturing the nonlinear characteristics of the flow fields of interest. With the actual modeling of blade rows in relative motion, this code is capable of computing the unsteady interactions between blade rows.

### A. Geometry & Operating Conditions

Several BLI inlet designs were tested in the NASA Langley Research Center 0.3-meter Cryogenic Wind Tunnel<sup>9</sup> to evaluate possible geometries for blended-wing-body (BWB) designs<sup>10</sup>. Using nitrogen injected as a cryogenic liquid into the closed loop system, realistic operating conditions of a BWB design at cruise were simulated. The inlet was a flush-mounted, S-duct design with large amounts of boundary layer ingestion. Experimental results include total pressure measurements from a fixed rake at the Aerodynamic Interface Plane (AIP), which represents the attachment point of the fan, static pressure measurements along the tunnel and inlet walls and a boundary layer rake. The inlet A geometry was selected to be modeled, which represents a more conservative lip thickness and semicircular throat aperture.

The test case selected for initial runs was at a moderate external Mach of 0.402. A higher external Mach of 0.805 was also selected, representing operating conditions close to cruise conditions. Both cases exhibited strong secondary flow structures in the experimental results. Table 1 provides operating conditions for both cases.

**Table 1. Operating conditions for validation cases**

$M_{\infty}=0.402$	$M_{\infty}=0.805$
$Re/ft = 52.03 \times 10^{-6}$	$Re/ft = 69.97 \times 10^{-6}$
$T_{t,\infty}=100 \text{ }^{\circ}\text{K}$	$T_{t,\infty}=100 \text{ }^{\circ}\text{K}$
$P_{t,\infty}=434,370 \text{ Pa}$	$P_{t,\infty}=351,632 \text{ Pa}$
$\dot{m}_{2c} = 0.4064 \text{ kg/s}$	$\dot{m}_{2c} = 0.4095 \text{ kg/s}$

Once the external and inlet flow modifications were validated against experimental data, a fan was attached to the inlet to test the ability of the modified TURBO to simulate the coupled problem. The fan geometry selected was a design used at NASA-Glenn for aero-acoustic testing (SDT2-R4) and has 22 blades<sup>11</sup>. To allow for qualitative analysis of the impact that a fan would have on the inlet flow field, the fan geometry was scaled down to match the diameter of the inlet. This will allow the total pressure distortion at the AIP observed without a fan present to be compared to the predicted flow field with a fan attached.

## B. Numerical method

Most turbomachinery applications that the TURBO code was developed to analyze are axisymmetric about the longitudinal axis. TURBO development has naturally paralleled this and most of the boundary conditions and user input parameters are geared towards axisymmetric geometries. Some modeling efforts<sup>12</sup> have employed independent grids for the fixed upstream inlet flowfield and the rotating grid of the fan section. A transfer mechanism was employed to interpolate and pass data between the two surfaces. For this effort it was decided to develop grids with the same concentric rings at the AIP interface, so that the sliding interface currently in TURBO could be utilized. This proven method maintains continuity at the interface between the fixed and rotating grids.

Choosing to match the grids at the AIP interface complicates meshing the upstream flowfield. A concentric mesh was selected for the fan and the mesh upstream of the AIP was fixed at this location and smoothed upstream to fit to the inlet and external geometry. This required that the centerline singularity that occurs at the nose of the spinner be extended upstream through the inlet and into the upstream flow. Figure 1 shows the overall model, which represents the complete test section from the experiment. Grid density is shown for the external region of the flow field and the inlet is shown as solid surfaces for clarity. The mesh contains a total of 31 million cells. 10

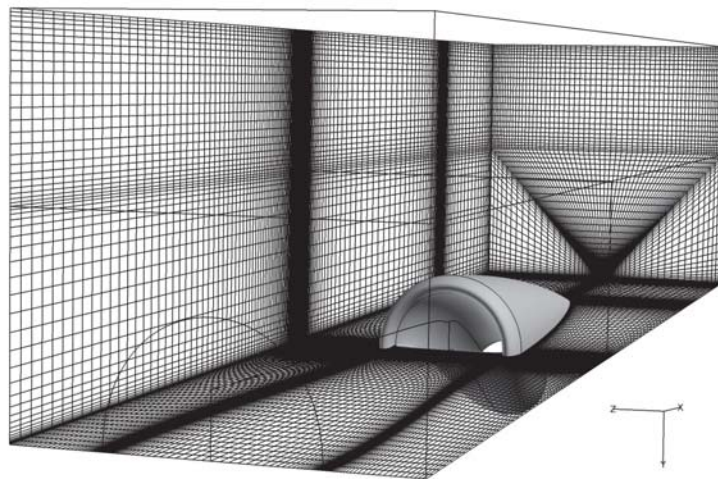


**Figure 1. Numerical mesh of test section and inlet**

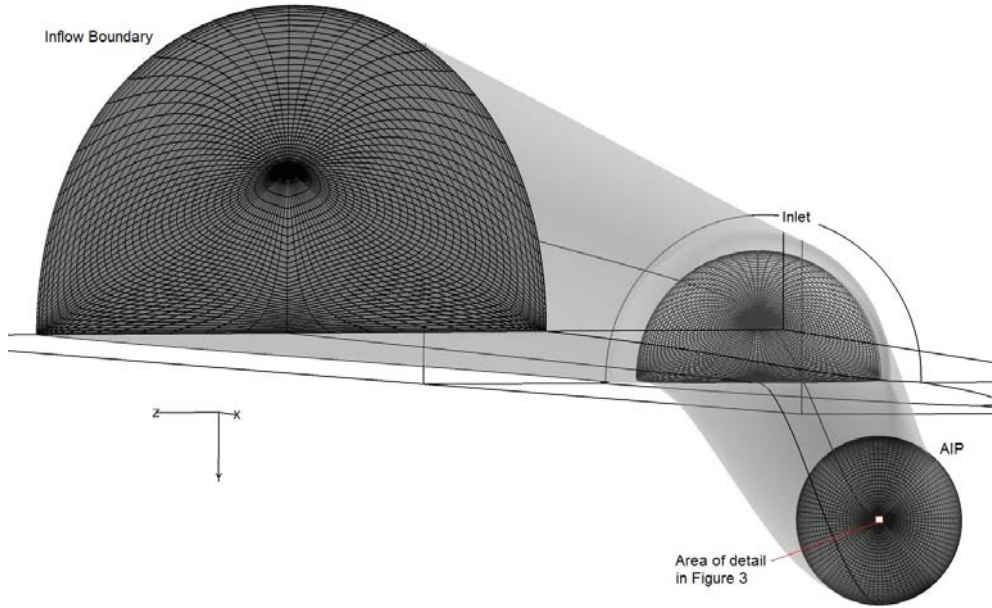


**Figure 2. Mesh sections that include centerline boundary**

million cells in the external flow, 2 million cells in the inlet section and 19 million cells in the full annulus rotor section.

Figure 2 shows the mesh sections from Fig. 1 that contains the centerline boundary. The concentric grid that is optimal for the fan section can be seen at the AIP and the centerline point is diagramed in Fig. 3. This is an optimal mesh for the rotating section and the inlet near the AIP, and maintains direct connectivity between the inlet and the fan sections. Transitioning this axisymmetric mesh into the semi-circular inlet and rectangular external flow is the primary difficulty with this technique. If a non-cylindrical mesh was used upstream of the AIP, a more appropriate mesh for that geometry could be obtained, but the mesh elements would not be aligned at the AIP interface and interpolation would be required to transfer flow properties across the boundary. The impact of interpolation on the numerical results is unknown at this time, and can be studied once results with the direct mapping are obtained. In Fig. 2 only half of the grid elements are displayed, to improve the visual quality of the grid.

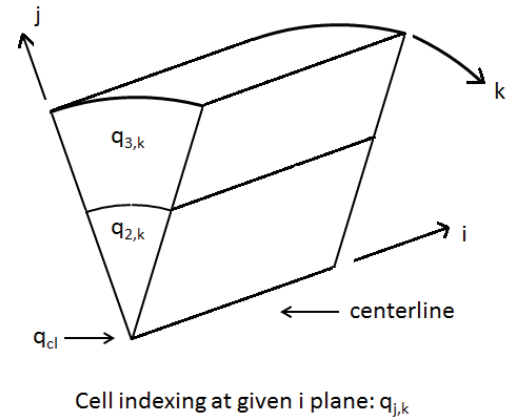


**Figure 3. Schematic of finite volume element at the centerline boundary**

A new boundary condition was created to handle the singularity at the centerline in the inlet and upstream flowfield in Fig. 2. In a finite difference methodology, the flow properties at the centerline node would simply be set to the same value, but the finite volume formulation of TURBO is cell centered and flow properties cannot be specified at the centerline point, point  $q_{cl}$  in Fig. 3. On all cells that are adjacent to the centerline, the face that lies on the centerline is collapsed and has an area of zero. This prohibits any flux from passing through that face into the cell directly across the centerline. At each  $i$  index, the new centerline boundary condition sets the value of each cell adjacent to the centerline,  $q_{2,k}$  so that  $q_{cl}$  would be the same for each element. The target value of point  $q_{cl}$  is set to the average of all of the elements surrounding the centerline, in equation (1).

A first order extrapolation is used to determine what the cell centered values of  $q_{2,k}$  should be to achieve the uniform condition of the target centerline point  $q_{cl}$ . Based on this value of  $q_{cl}$  and the 2<sup>nd</sup> radial element,  $q_{3,k}$ , an updated value of  $q_{2,k}$ , given in equation (2), can be computed. The new value of  $q_{2,k}$  for each cell surrounding the

$$q_{cl} = \frac{\sum_{k=2}^{nk} q_{2,k}}{nk-1} \quad (1) \quad q_{2,k} = \frac{2}{3} q_{cl} + \frac{1}{3} q_{3,k} \quad (2)$$

the centerline helps communicate flowfield data to elements around the centerline.

When used with the local time stepping feature of TURBO enabled, which sets the local timestep of each block to be based on a user selected CFL value, the centerline boundary condition was required to achieve convergence. When used with the local time stepping feature disabled, a time accurate solution is obtained with the entire domain solved with a fixed timestep and the centerline boundary condition provided improved convergence and minimized distortions at the centerline.

### C. Turbulence Model

The turbulence model used to generate these results is a two equation k-epsilon model that uses a wall function approximation to compute flow properties near the wall.  $y^+$  values for cells along the bottom walls of Fig. 2 are in the 30 to 100 range upstream of the AIP. Third order accurate spatial discretization was specified along with 2<sup>nd</sup> order accurate in time.

### D. Inflow Boundary Conditions

In the experimental test facility, the flow enters the test section from a 90° elbow and passes through a screen, resulting in an unknown, but established boundary layer entering the straight test section. The length of the domain modeled upstream of the inlet in Fig. 2 is not enough to allow the boundary layer to fully develop. Increasing the distance from the inflow boundary to the inlet was felt to be too computationally expensive and would still be an approximation, since that does not match the physical facility. It was decided to provide a flow profile that includes a fully developed boundary layer as an inflow boundary condition. An iterative approach was selected where the solution was started with a uniform inflow boundary. After the unsteady solution was determined to be converged, flow properties on a plane perpendicular to the axial direction, approximately 40% between the inflow boundary and the inlet entrance, were extracted and stored. The solution was restarted with this profile specified as the inflow profile. This process was repeated until the boundary layer thickness matched that from the experimental results. It will be shown that this method provides a boundary layer profile similar to that in the experiment.

### E. Outflow Boundary Conditions

Existing TURBO boundary conditions were utilized at the outflow boundaries, but code modifications were required to allow for two outflow boundaries to operate concurrently. For the freestream outflow, a subsonic characteristic variable outflow boundary was specified, because the external flow at the exit plane downstream of the inlet remains subsonic for both the  $M_\infty=0.402$  and  $M_\infty=0.805$  cases. Static pressure is prescribed at this boundary, but this value was not reported in the experimental data. Since the external flow velocity in the tunnel section upstream of the inlet will be dependent on the value of pressure set at the exit, an estimate was used initially and refined until a computed freestream velocity was obtained that matches the value measured in the experiment.

For the inlet only simulations, corrected mass flow values for the inlet at the AIP were available from the experimental data. Since no fan was attached to the AIP interface, a mass flow boundary condition was selected at the AIP interface and the corrected mass flow reported from the experimental results was specified. When the fan section was attached, a sliding boundary condition was applied to the inlet and rotor blocks at the AIP and the mass flow exit boundary condition was moved to the exit plane downstream of the fan.

## III. Results and Discussion

The primary objective of this effort was to validate the TURBO modifications for solution of the flow field upstream of the AIP. As discussed in section II D, the inflow boundary profile for each case was obtained by running the solution several times and updating the inflow profile until an established boundary layer was present. Time accurate solutions were computed for the two operating conditions given in Table 1. To compare against experimental data, the unsteady numerical results were averaged from 20 data samples over a time period of 1.14 seconds obtained after the flow was determined to have reached a steady state. Averaged results were computed for static pressure profiles down the tunnel wall, down the inlet lower wall, total pressure profile in the boundary layer

near the inlet and total pressure distributions at the AIP. Averaged results are then compared to experimental results.

The secondary objective was to attach the fan geometry, scaled down to match the geometry of the inlet, and obtain simulations run at the same operating conditions in Table 1, along with a fan RPM adjusted for the change in scale. This will both document the behavior of the coupled inlet/fan solution and allow some qualitative analysis of the impact that the fan has on the upstream flow field.

#### A. External and Inlet Flow Validation

With boundary conditions set to simulate the  $M_\infty=0.402$  case with a corrected mass flow at the AIP of 0.4064 kg/s, a solution was obtained that resulted in an external flow velocity of  $M_\infty=0.403$  in the tunnel section upstream of the inlet. Corrected massflow at the AIP was computed to be 0.6% higher than the experimental value. Figure 4a shows the Mach number contours on the mid-plane of the averaged flowfield.

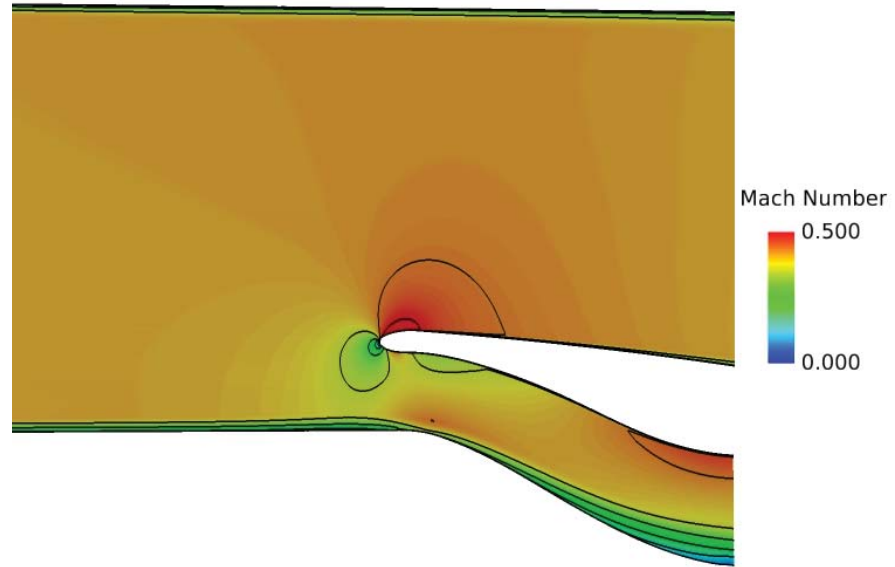


Figure 4a. Mach contours, computed  $M_\infty=0.403$

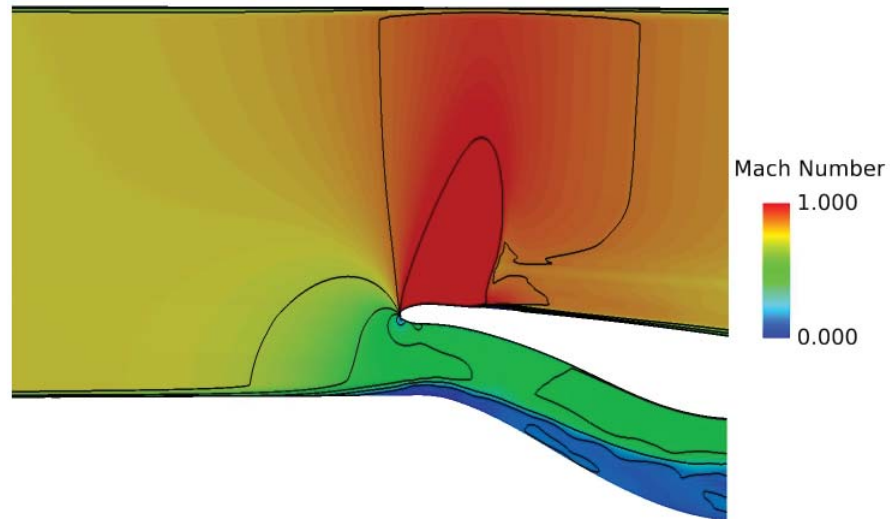
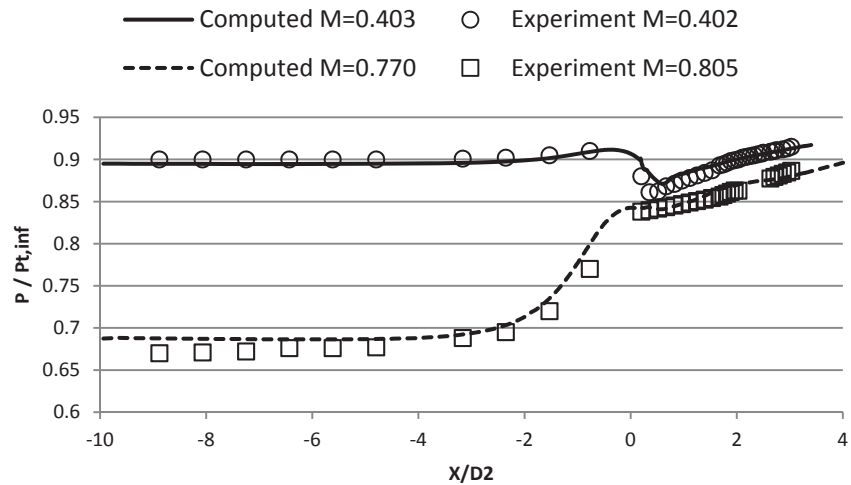


Figure 4b. Mach contours, computed  $M_\infty=0.770$

of the averaged flowfield. With the capture area of the inlet larger than the free stream area of the streamtube, yielding an area ratio of  $A_o/A_c=0.771$ , some of the external flow bypasses the inlet as spillage and the flow entering the inlet decelerates slightly. The secondary flow structure that evolves in the serpentine inlet, due to the convective derivative term in the vorticity rate of change equation<sup>13</sup>, collects the boundary layer on the bottom wall of the duct. The low momentum region that develops can be seen growing in thickness as the flow progresses axially. The secondary flow migrates the low momentum fluid up towards the center of the duct and this establishes the distorted flow field at the AIP that the fan will interact with.

For the experimental case with  $M_\infty=0.805$  and corrected mass flow at the AIP of 0.4095 kg/s, the numerical solution yielded an external flow of  $M_\infty=0.770$ , which is about 4.4% lower than the experimental target. This was a result of having to specify a static pressure at the external flow outlet that partially defines the external flow velocity. This information was not available in the reported data, so an estimate was used. Corrected massflow was closer and computed to be 0.5% over the experimental value. At these operating conditions, the flow in the inlet was found to become turbulent downstream of the inlet entrance. Figure 4b shows Mach contours of the averaged flow field. Some of the unsteadiness can still be seen in the averaged data, but it shows the growth of the low momentum

flow along the bottom of the inlet. The depth of the low momentum region at the AIP is thicker for the  $M_\infty=0.770$  case, compared to the  $M_\infty=0.403$  case. With the experimental mass flows given in Table 1 for both cases within 1% of each other, the velocities in the inlet are expected to be of similar magnitudes. In Fig. 4b the flow experiences a greater deceleration as it approaches the inlet, compared to Fig. 4a.



**Figure 5. Tunnel and inlet duct normalized static wall pressure**

To quantitatively validate the accuracy of the model, Fig. 5 compares the experimentally measured normalized static pressure  $P/P_{t,\infty}$  along the bottom of the tunnel wall and the bottom of the inlet, with the averaged numerical results. The distance  $x/D2=0$  represents the inlet entrance, with negative values representing locations upstream of the inlet. For the  $M_\infty=0.403$  solution, computed results match very well. Far upstream of the inlet, the computed pressure is about 0.6% lower than experimental data. This is because the computed external velocity is slightly higher. Pressure calculations just downstream of the inlet report the highest error, differing from experimental values by about 2.5%. The exact cause for this discrepancy was not identified, but results indicate that refinement of the turbulence model parameters should improve accuracy in this region. The solution recovers and after the midpoint of the inlet, the pressure matches data very well.

In the experiment, the  $M_\infty=0.805$  case was run over a range of inlet massflow values. Static wall pressure data indicates that this test case is right at the transition point between attached and separated flow in the inlet, as massflow values below the test case show smooth increases in static pressure and massflow values above the test case show a sharp dip in static pressure just downstream of the inlet. TURBO was able to replicate this behavior. With the computed massflow within 0.5% of the experimental value, static pressure values predicted downstream of the inlet match well, given they are averaged. The solution upstream of the inlet over predicts the static pressure by about 2.5%, due primarily to the difficulty selecting the correct external flow backpressure.

A boundary layer rake was employed in the experiment to obtain boundary layer profile information near the inlet. The boundary layer rake was located at the same axial location as the inlet,  $x/D2=0$ , and was situated to the side of the inlet, to avoid disturbing the flow entering the inlet. Fig. 6 presents the boundary layer profile measured and computed. For the  $M_\infty=0.403$  case, results show that the boundary layer thickness is accurately modeled, but the profile close to the wall is not fully captured. The  $y^+$  values for this mesh are in the range of 30 to 100, which represents a somewhat coarse mesh. The results from the  $M_\infty=0.770$  case indicate a similar

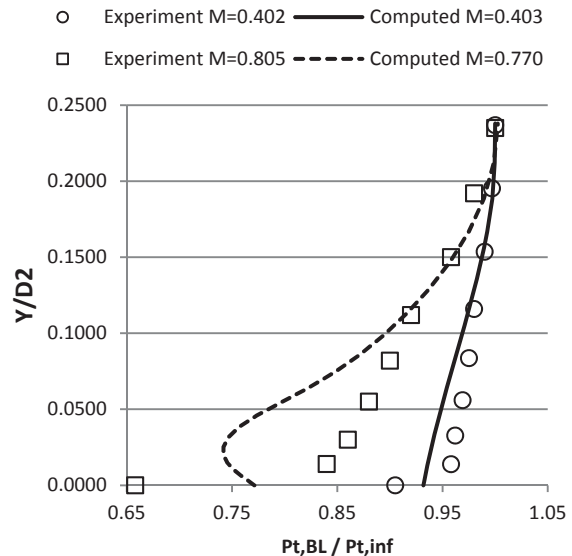


**Figure 6. Boundary layer profile**

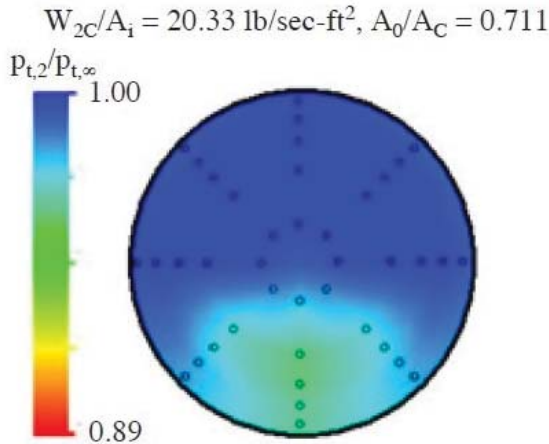


Figure 7a. Experimental  $P_t/P_{t,\infty}$  at AIP,  $M=0.402$

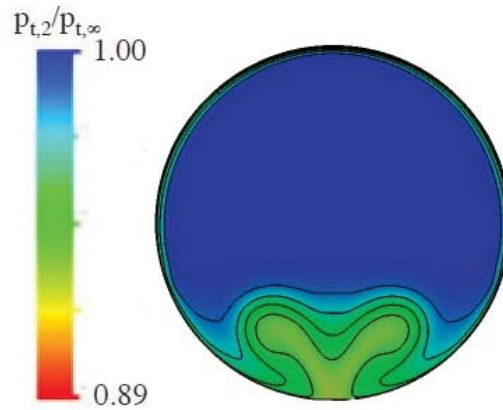


Figure 7b. Computed  $P_t/P_{t,\infty}$  at AIP,  $M=0.403$

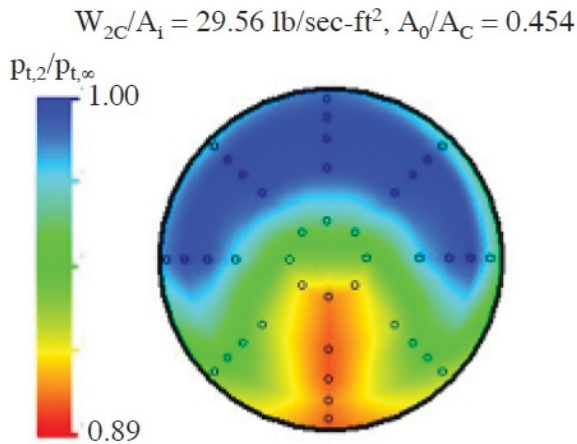


Figure 8a. Experimental  $P_t/P_{t,\infty}$  at AIP,  $M=0.805$

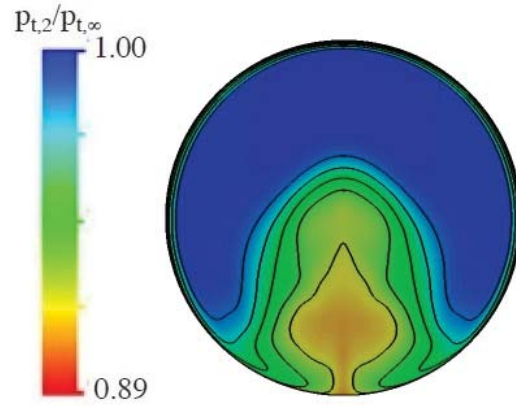


Figure 8b. Computed  $P_t/P_{t,\infty}$  at AIP,  $M=0.770$

trend. The boundary layer thickness is captured, but the total pressure profile within the boundary layer is under-predicted. It was discussed in section II D that since the boundary layer profile at the inflow boundary cannot be modeled exactly, an approximation was specified. Obtaining a realistic total condition and velocity profile at the inflow boundary is important to establishing a correct boundary layer thickness at the inlet.

Of primary interest to the present work is the accuracy of the solution at the AIP, as this will be the flow distortion presented to the fan. Figure 7a shows the normalized total pressure measured at the AIP for the experimental  $M_\infty=0.402$  case. The small circles represent the location of the total pressure probes in the fixed rake. Figure 7b shows the computed results and the secondary flow structure established by the S-duct geometry. The total pressure distortion matches very well with the experimental data, with the overall profile as well as the magnitude captured. The computed flow field provides a much higher resolution than the experimental results, which are interpolated data based on the 40 point total pressure probe rake. The additional vortex characteristics predicted by the simulation, while matching the overall structure, cannot be confirmed due to the lower resolution of the experimental data.

One interesting trend observed was how the total pressure distribution computed at the AIP matches the experimental results well, comparing Fig. 7a and Fig. 7b, but the total pressure profiles within the boundary layer seen in Fig. 6 show differences between the computed and experimental results. It was theorized that matching the boundary layer thickness in the external flow is of primary significance when trying to accurately predict the total pressure distribution at the API, and the solution is less sensitive to the predicted profile within the boundary layer.

To evaluate this, several solutions were obtained with similar external flow properties, but different boundary layer profiles upstream of the inlet for the  $M_\infty=0.403$  case. Figure 9, which is similar to Fig. 6 but with an enlarged  $P_t$  scale, shows four boundary layer profiles at the inlet, computed at the location of the boundary layer rake. Figure 10 shows the corresponding total pressure distortions observed at the AIP for each case. Case #1 in Fig. 9 yields a boundary layer about 35% thinner than the thickness measured experimentally, and cases #2 through #4 provide improved solutions. While case #4 affords the best BL thickness match, it under-predicts the total pressure distribution within the boundary layer. Case #1 in Fig. 9 over predicts the total pressure distribution within the boundary layer by about the same amount that case #4 under-predicted. It can be seen in Fig. 10 that the solution provided by case #4 results in a total pressure distortion that matches the experimental results, while the distortion computed with case #1 was significantly different. These results indicate a strong relationship between the upstream boundary layer thickness and the total pressure distortion predicted at the AIP and less of a dependency on the profile within the boundary layer.

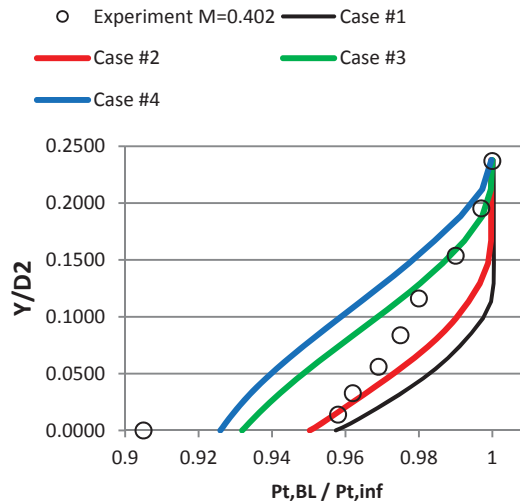


Figure 9. Four different BL profiles at the inlet

Figure 8b shows the total pressure distortion computed for the  $M_\infty=0.770$  case. As seen in Fig. 6, the boundary layer currently computed by this case matches the thickness well. In line with the comments about the importance of accurately predicting the boundary layer thickness, the total pressure distortion at the AIP matches reasonable well. The averaged results of the turbulent flow show the distortion to be larger than the low speed case due to the fluctuations. Additional details of the vortex structure can be seen in the computed results which match the overall vortex size, structure and magnitude.

## B. Inlet/Fan Interaction Modeling

With the TURBO modifications for the upstream flow validated, the sliding boundary interface already built into TURBO was used to attach the fan geometry to the inlet to provide simulation of the coupled upstream inlet flow and rotating fan section. The fan geometry was scaled to match the experimental inlet A dimensions so that the impact of the fan on the experimental data could be observed. Since the size of the fan was changed, design operating conditions for the geometry no longer existed and hypothetical operating conditions were selected. A fan RPM of 45,000 was selected to try to match the relative flow angles seen in simulations of the full size fan, which rotates at 12,657 RPM.

Figure 11 shows the computed Mach contours through the inlet and fan sections for the  $M_\infty=0.403$  case. Four fan revolutions were allowed to complete, at which time the unsteady solution was determined to have reached steady state. In addition to confirming that the combined model is able to successfully couple the upstream flow distortion to the fan, some qualitative insight is gained into the effect that the fan has on the upstream flowfield.

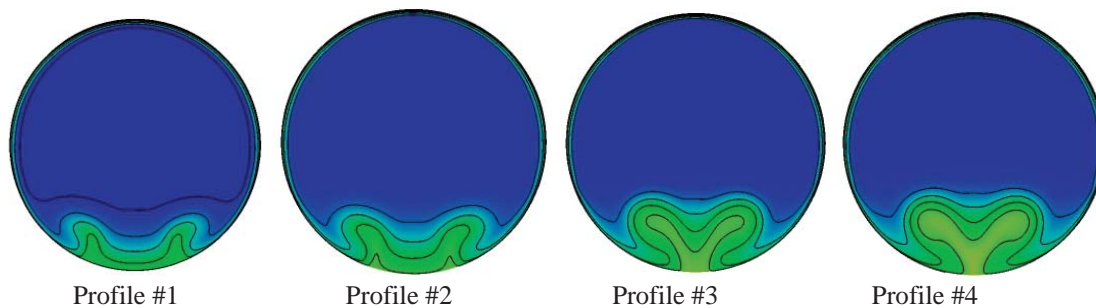
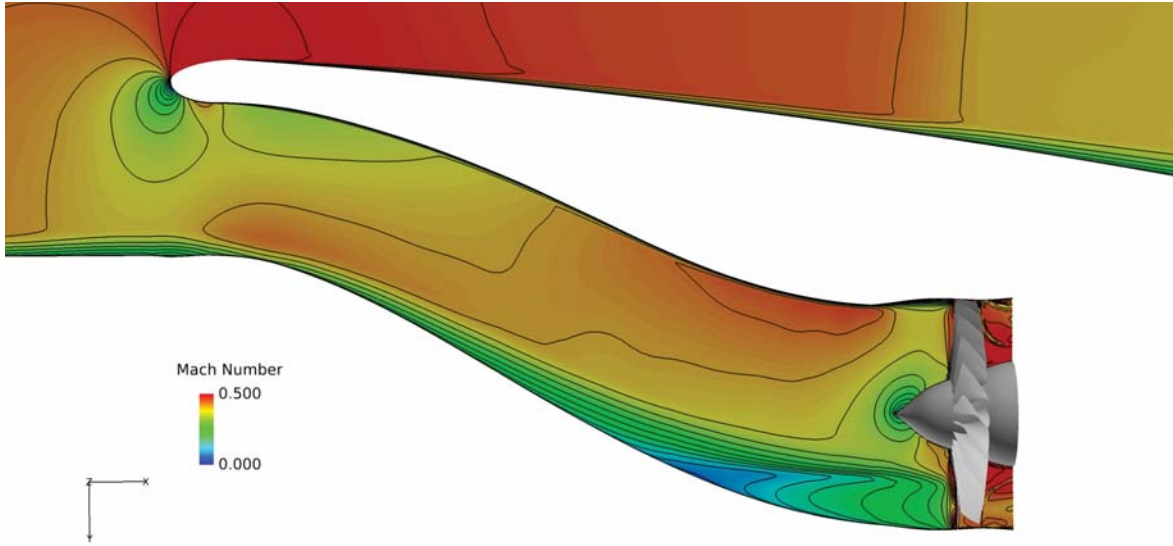


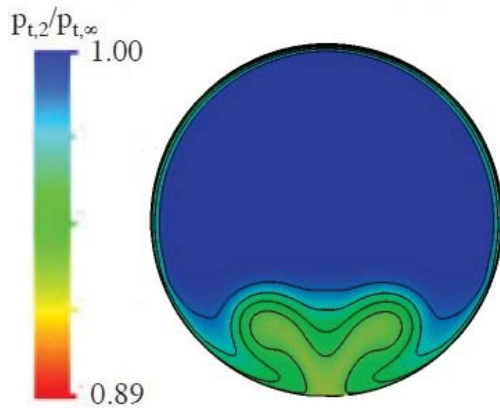
Figure 10.  $P_t/P_{t,\infty}$  at the AIP for four different boundary layer profiles



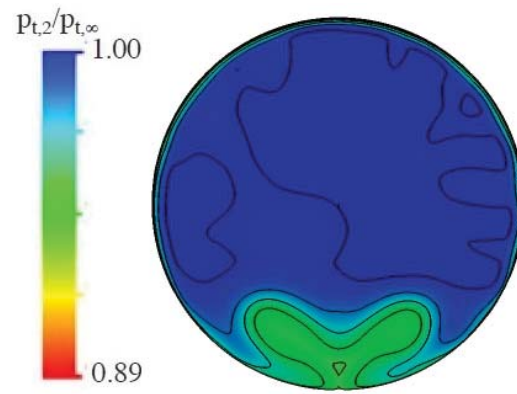
**Figure 11. Mach number profiles of combined inlet / fan solution,  $M_\infty=0.403$**

Figure 12a shows the total pressure distortion at the AIP computed without the fan, and Fig. 12b shows the distortion computed at the AIP with the fan present. Results in Fig. 12b are averaged so some of the instantaneous flow properties due to the influence of the fan are averaged out, but the distortion can be seen to be reduced in height a small amount. Also noted is the reduction of total pressure loss compared to the inlet only case. However, overall the secondary flow structure seems to be unaffected by the presence of the fan.

To examine how the distortion evolves through the blade passages, total pressure in the absolute reference frame is used. This parameter is chosen because it correlates and tracks the evolution of the inlet distortion. Figure 13a through 13e show the absolute total pressure distribution, at a specific instance in time. Figure 13a is at a plane half way between the nose of the spinner and the leading edge of the blade row. Figure 13b through 13d are planes located at 15%, 50%, and 80% blade chord, respectively, and Figure 13e is at the exit of the fan section. Figure 13a shows that past the nose of the spinner, the low total pressure distortion remains largely intact and located at the bottom of the duct. The distortion then transferred to the bottom of the fan blades at 15% chord, highlighted in the black box in Fig. 13b. The low total pressure has not experienced a circumferential displacement from where it was observed upstream of the spinner. This is evidenced by the relatively lower total pressure on the suction surface of the bottom blades as compared to elsewhere in the fan. Additionally, it is noted in this area the total pressure on the pressure surface is higher on the right side blades than those on the left side blades. The cause of this asymmetry will be examined in more detail later. Moving down to 50% chord in Fig. 13c there is not much apparent feature to distinguish the distortion. But if examined closely, the total pressure level on the lower left side is lower than elsewhere. The same low total pressure region is more clearly seen at 80% chord in the black box in Fig. 13d. Note



**Figure 12a.  $P_t/P_{t,\infty}$  without fan**



**Figure 12b.  $P_t/P_{t,\infty}$  with fan**

that this low total pressure region stays in the same circumferential location from 15% chord to 80% chord, indicating no circumferential displacement of total pressure distortion while the distortion propagates through the fan. Finally, at the exit plane in Fig. 13e, a vaguely low total pressure region can be seen in the same general bottom area. The total pressure level is not too much different from the rest of the flow field, indicating extra energy input to the distorted region as compared to the rest of the flow field, which attenuates the distortion. Overall, it is observed that as the inlet total pressure distortion propagates through the fan it 1) does not shift in circumferential direction, 2) exhibits asymmetry in the distorted region from the symmetric pattern at AIP, and 3) is attenuated. In the following, we offer explanations of the physical mechanism to these phenomenons.

Many numerical studies of the transfer of inlet total pressure distortion through fan/compressor have reached a similar conclusion that the distortion does not shift in circumferential direction. For example, Florea, etc. al.<sup>14</sup> indicated when the inlet is coupled with a fan; the inlet distortion propagates through the fan with little or no mixing at all. Yao, etc. al.<sup>3</sup> performed the simulation of a one-per-rev inlet distortion through two 3-stage compressors and found no displacement of total pressure although total temperature does experience a circumferential displacement. They attributed the total pressure non-displacement as a result of zigzagging opposite circumferential phase shift in static pressure as the distortion passes through the three stages, and that circumferential phase shift is not a literal shift driven by flow particles but rather, the result of pressure and temperature rise caused by the blades operating at respective inlet and discharge conditions that vary in circumferential direction. Similar explanations can be applied to our case so the details will not be repeated here. Rather, we will focus on the explanation of total pressure distortion asymmetry and its attenuation.

To explain these two phenomenons, the relative flow incidence to the blades is analyzed. This is because incidence affects blade loading and can be used to understand the level of energy input to the flow as the distortion moves through the fan. Figure 14 shows the computed incidence distribution at the entrance face of the fan. It can be seen the incidence has an asymmetric pattern in the lower half of the face. This asymmetry is caused by the distortion and is best understood through the analysis of velocity triangles. Figure 15 indicates the flow orientation from the distortion vortex. Notice the counter-rotating vortex A and B of the distortion induces opposite tangential velocity  $u$  for flow entering the fan. When combined with the blade rotating speed, vortex A acts to decrease the tangential velocity, which decreases incidence of blades to the left side of the fan. On the contrary, vortex B increases the tangential velocity, hence increases the incidence of blades to the right side of the fan. This mechanism generates the incidence asymmetry in the area affected by the distortion vortex. Also note the high incidence at tip region; indicating the fan is also tip-loaded.

The incidence distribution is now used to explain how the blades respond to the distortion in terms of blade loading based on one simple rule: high incidence generates high loading, providing the incidence does not cause stall. Back to the black box in Figure 13b, the generally high incidence in this area (see Figure 14) generates high blade loading, which is reflected by the sharp difference in total pressure level between the pressure and suction surfaces of each blade. In the meantime, the asymmetry of incidence in the bottom region also imposes different loading with higher loading on the right side blades than the left side blades, which results in the observed pressure surface total pressure asymmetry among the blades in this region. Finally, the incidence asymmetry corresponds well to the asymmetric distribution of total pressure level in the lower half of Figure 13c and 13d in that the blades on the right pump in more energy than the blades on the left.

To understand the flow mechanism of the attenuation of total pressure distortion in Figure 13e, it is noted that the shape of the bottom high incidence of Figure 14 matches almost exactly to that of the bottom distortion in Figure 13a. The reason is that the axial velocity in the distorted region is low compared to other places (see Figure 11) and when combined with tangential velocity, it results in higher incidence. This higher incidence in turn enables more energy input to this area, which replenishes the low energy region of the distortion and raises the total pressure level in the distorted region to almost the same as the rest of the flow when it exits the fan. One important implication of this understanding is that this attenuation mechanism comes naturally as long as there is velocity deficit in the distortion and may be exploited for designing distortion tolerant fans for BLI applications.

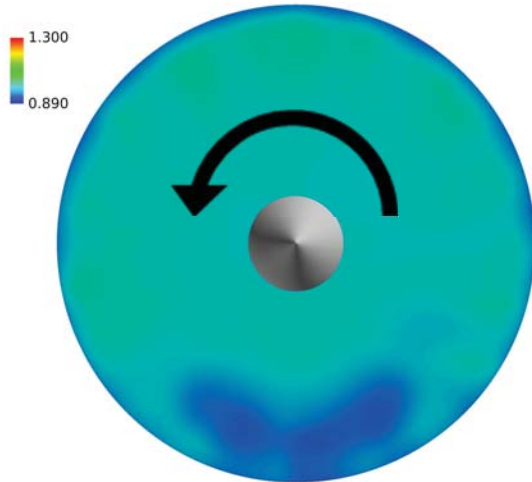


Figure 13a.  $P_t/P_{t,\infty}$  at 50% between spinner nose and blade leading edge

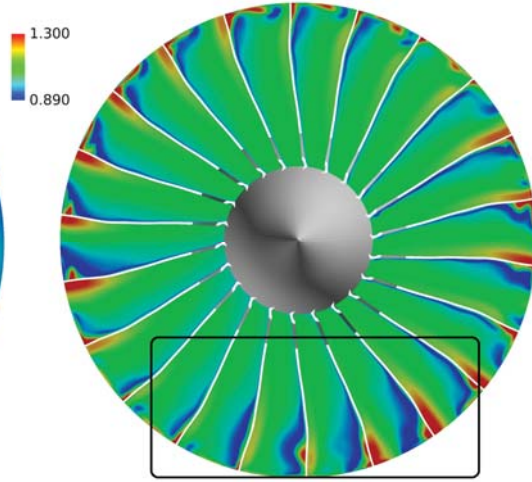


Figure 13b.  $P_t/P_{t,\infty}$  at 15% blade chord

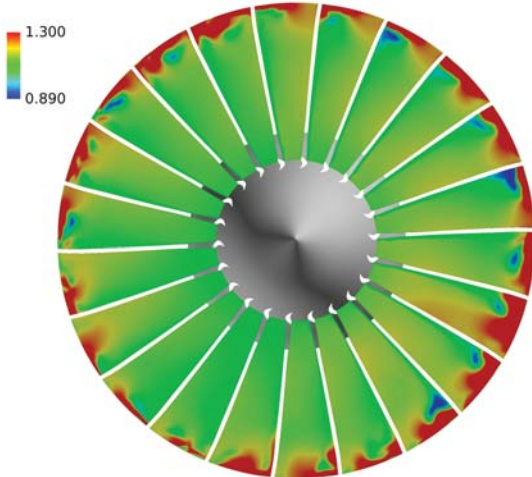


Figure 13c.  $P_t/P_{t,\infty}$  at 50% blade chord

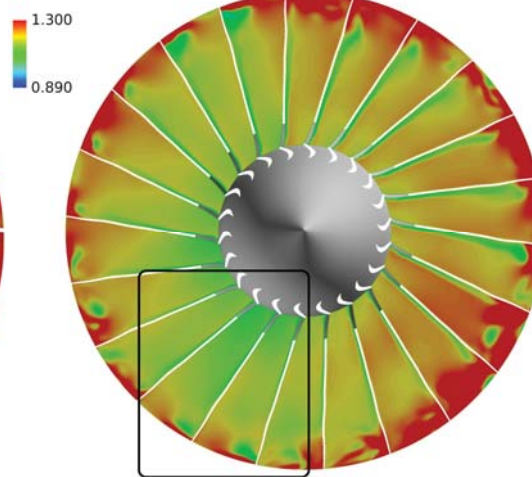


Figure 13d.  $P_t/P_{t,\infty}$  at 80% blade chord

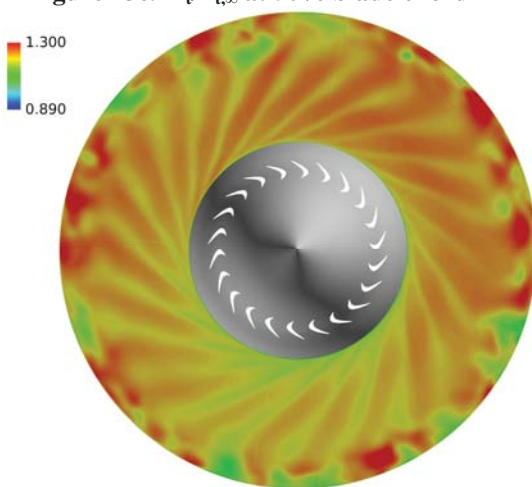


Figure 13e.  $P_t/P_{t,\infty}$  at exit plane

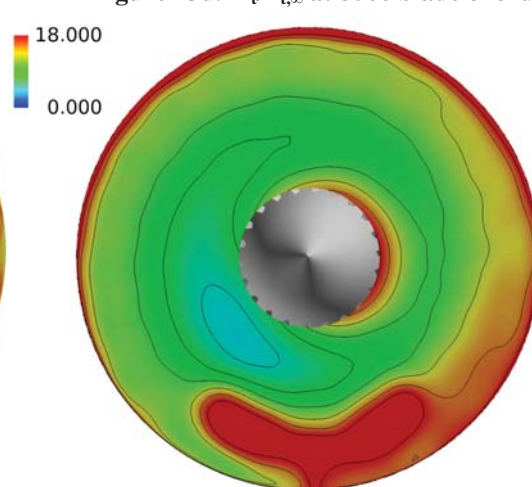


Figure 14. Flow incidence angle



Glenn). This work was supported in part by an allocation of computing time from the Ohio Supercomputer Center under project PAS0239.

## References

- <sup>1</sup> Smith, L. H., "Wake Ingestion Propulsion Benefit," *Journal of Propulsion and Power*, Vol. 9, No. 1, 1993, pp.74-82
- <sup>2</sup> Plas, A. P., Sargeant, M. A., Crichton, D., Greitzer, E. M., Hynes, T. P., Hall, C. A., 2007, "Performance of a Boundary Layer Ingesting (BLI) Propulsion System," *AIAA Journal*, AIAA 2007-450,
- <sup>3</sup> Jixian Yao, Steven E. Gorrell and Aspi R. Wadia, "High-Fidelity Numerical Analysis of Per-Rev-Type Inlet Distortion Transfer in Multistage Fans—Part II: Entire Component Simulation and Investigation," *ASME Journal of Turbomachinery*, Vol. 132, No. 4, 041015 (17 pages), May, 2010
- <sup>4</sup> List, M.G., Howard, R.M., "Investigation of Total Pressure and Swirl Distortion in a Single-State Transonic Fan", *2012 High Performance Computer modernization Program Contributions to DoD Mission Success*, September, 2012.
- <sup>5</sup> Chima, R.V., Arend, D.J., Castner, R.S., Slater, J.W., Truax, P.P., "CFD Models of a Serpentine Inlet, Fan, and Nozzle," *NASA*, NASA/TM 2010-216349, May 2010
- <sup>6</sup> Allan, B.G. Owens, L.R., "Numerical Modeling of Flow Control in a Boundary-Layer-Ingesting Offset Inlet Diffuser at Transonic Mach Numbers," *44<sup>th</sup> AIAA Aerospace Sciences Meeting*, Reno, NV, 2006
- <sup>7</sup> Chen, J. P., and Whitfield, D. L., "Navier-Stokes Calculations for the Unsteady Flowfield of Turbomachinery," *AIAA Conference*, AIAA 93-0676,
- <sup>8</sup> Berrier, B. L., Allan, B. G., "Experimental and Computational Evaluation of Flush-Mounted, S-Suct Inlets," *42<sup>nd</sup> AIAA Aerospace Sciences Meeting*, Reno, NV, 2004
- <sup>9</sup> Mineck, Raymond E.; and Hill, Acquilla S., "Calibration of the 13- by 13-Inch Adaptive Wall Test Section for the Langley 0.3-Meter Transonic Cryogenic Tunnel," *NASA*, NASA Technical Paper 3049, December 1990
- <sup>10</sup> Berrier, B. L., Carter, M. B., Allan, B. G., "High Reynolds Number Investigation of a Flush-Mounted, S-Duct Inlet With Large Amounts of Boundary Layer Ingestion," *NASA*, NASA Technical Paper 2005-213766, September 2005
- <sup>11</sup> Woodward, R. P., and Hughes, C. E., "Noise Benefits of Increased Fan Bypass Nozzle Area," *NASA/TM-2004-213396*, November, 2004.
- <sup>12</sup> Webster, R. S, Sreenivas, K., Hyams, D. G., Hilbert, C. B., Briely, W. R., and Whitfield, D. L., "Demonstration of Sub-system Level Simulations: A Coupled Inlet and Turbofan Stage," *AIAA/ASME/SAE/ASE Joint Propulsion Conference*, AIAA 2012-4282, Atlanta, GE, 2012
- <sup>13</sup> Greitzer, E.M., Tan, C.S., and Graf, M.B., *Internal Flow: Concepts and Applications*, Cambridge University Press, Cambridge, England, 2004.
- <sup>14</sup> Florea, R.V., Voytovych, D., Tillman, G., Stucky, M., Shabbir, A., Sharma, O., and Arend, D.J., "Aerodynamic Analysis of A Boundary-Layer-Ingesting Distortion-Tolerant Fan," *IGTI paper GT2013-94656*, June 2013